Fuel Processing Technology 286 (2026) 108442

Contents lists available at ScienceDirect

Fuel Processing Technology

journal homepage: www.elsevier.com/locate/fuproc

Research article

Decoupling the injection strategy-dependent regulation mechanisms of methanol on Ammonia/diesel combustion under medium load

Jingrui Li [a,*], Sijie He [a], Guyu Feng [a], Changchun Xu [a], Haifeng Liu [b], Xinyan Wang [c], Hua Zhao [c]

[a] School of Energy and Power, Jiangsu University of Science and Technology, Zhenjiang 212013, China
[b] State Key Laboratory of Engine, Tianjin University, Tianjin 300350, China
[c] Center for Advanced Powertrain and Fuels, Brunel University London, London UB8 3PH, UK

ARTICLE INFO

Keywords:
Ammonia/diesel dual-fuel engine
Methanol blending
Injection strategy
Thermal quenching
Chemical kinetics

ABSTRACT

Ammonia is a promising zero-carbon fuel, yet its application is hindered by low flame speed and high ignition energy. While methanol serves as a high-reactivity additive, its effectiveness strongly depends on operating strategies, particularly under medium-load conditions where chemical enhancement competes with physical cooling. This study employs a validated 3D-CFD model to reveal the dual effects of diesel start of injection (SOI) and methanol energy fraction (MEFP) on an ammonia/diesel engine with 90% ammonia energy fraction. Results demonstrate that SOI dictates whether methanol acts as a promoter or inhibitor. At early SOI (−18 °CA ATDC), methanol exhibits a non-monotonic effect: it initially promotes combustion but triggers severe deterioration when MEFP exceeds 40%, primarily due to thermal quenching of the diesel ignition kernel by the high latent heat of methanol. Conversely, late SOI (−14.2 °CA ATDC) creates a thermodynamic state that counteracts this cooling, allowing methanol to consistently enhance reactivity. An optimal configuration was identified at late SOI with 10% MEFP, achieving 43.3% thermal efficiency, reducing unburned NH_3 by 97%, and maintaining near-zero NO. Chemical kinetic analysis confirms that performance collapse is driven by a severe spatial disconnect between fuel-rich regions and the OH radical pool.

1. Introduction

Global decarbonization strategies have accelerated the transition of internal combustion engines toward carbon-neutral fuels [1–4]. While electrification is viable for light-duty vehicles, heavy-duty transport and marine propulsion require high-energy-density liquid fuels. Ammonia (NH_3), characterized by its carbon-free structure and established infrastructure, has emerged as a leading candidate for these sectors [5]. However, the practical application of ammonia is severely constrained by its high auto-ignition temperature and low laminar flame speed, which often lead to unstable combustion and excessive unburned NH_3 emissions [6].

To address these limitations, the ammonia/diesel dual-fuel (ADDF) combustion mode has been widely adopted [6–8]. In this mode, a high-reactivity pilot fuel (diesel) ignites the premixed ammonia. Previous studies indicate that while ADDF engines can achieve diesel-like efficiency at low-to-medium ammonia energy fractions (AEF), performance deteriorates significantly when the AEF exceeds 80% [9–12]. High AEFs result in global temperature reduction and prolonged combustion duration, causing a surge in unburned ammonia and N_2O emissions. Although optimizing the start of injection (SOI) [13–15] and employing split injection [16–19] can mitigate these issues to some extent, their effectiveness is limited under high-AEF conditions due to the inherent low reactivity of the mixture. To mitigate these issues, optimizing injection strategies has become a primary research focus. Recent studies have demonstrated the potential of advanced injection techniques.

Consequently, blending high-reactivity additives into ammonia has been proposed. While hydrogen and methane are effective [20–22], their storage and supply complexity limit practical utility. Methanol, being a liquid fuel with high reactivity relative to ammonia (though less reactive than diesel) and good miscibility, offers a superior logistical solution. Recent studies have further emphasized the importance of injection strategies in ammonia engines. For instance, the role of ammonia combined injection [23], the effects of injection pressure and nozzle dimension [24], and the spatial modification of ammonia injectors [25] have been investigated to improve combustion and emissions. However, a critical knowledge gap remains regarding the coupling effect of methanol addition under medium-load conditions. Preliminary studies

* Corresponding author.
E-mail address: lijingrui@just.edu.cn (J. Li).

https://doi.org/10.1016/j.fuproc.2026.108442
Received 16 January 2026; Received in revised form 12 March 2026; Accepted 23 March 2026
Available online 27 March 2026

Table 1
Main specifications of Caterpillar 3401 diesel engine.

Parameters	Value
Type	Caterpillar 3401
Number of cylinders	1
Bore	137.2 mm
stroke	165.1 mm
Connecting rod	261.62 mm
Compression ratio	16.25
Maximum power output	74.6 kW
Engine speed at full load	2100 rpm
Intake valve opening	−358.3 °CAATDC
Intake valve closing	−169.7 °CAATDC
Exhaust valve opening	145.3 °CAATDC
Exhaust valve closing	348.3 °CAATDC

Table 2
Physicochemical properties of diesel, ammonia, and methanol.

Property	Diesel	Ammonia	Methanol
Chemical Formula	$C_{10}H_{22}$ (approx)	NH_3	CH_3OH
Lower Heating Value (MJ/kg)	42.5	18.6	19.9
Latent Heat of Vaporization (kJ/kg)	270	1370	1103
Density (kg/m^3)	830	682	792

[26] have shown that methanol can enhance the combustion process of ammonia. However, current research has predominantly focused on high-load conditions, where high in-cylinder temperatures naturally facilitate combustion. A critical knowledge gap exists regarding medium-load operation, a common condition for marine and heavy-duty engines. At medium loads, lower in-cylinder temperatures may amplify the competition between chemical enhancement of ammonia and its high latent heat cooling effect, potentially altering the combustion mechanism observed at high loads.

Unlike previous studies that predominantly focus on high-load conditions where high in-cylinder temperatures naturally mask ignition difficulties, this study aims to bridge the knowledge gap regarding medium-load operation—a critical boundary where the competition between chemical enhancement and physical quenching is most acute. This work numerically investigates the coupled effects of SOI and Methanol Energy Fraction in Premixed fuel (MEFP) on an ADDF engine with a high AEF of 90%. The novelty of this research lies in identifying the non-monotonic “tipping point” of methanol's effect and establishing a theoretical framework that decouples the thermodynamic cooling penalty from the chemical reactivity benefit. By clarifying these competing mechanisms, this study provides precise guidance for the thermal management of triple-fuel combustion systems.

2. Numerical method

2.1. Test engine

The numerical investigation was performed based on a Caterpillar 3401 single-cylinder, four-stroke heavy-duty diesel engine [27]. The main specifications are listed in Table 1. The engine has a compression ratio of 16.25, and the diesel injector, located at the cylinder head center, features 6 holes with a diameter of 0.23 mm. To ensure proper atomization and targeting, the injection pressure is set to 50 MPa, and the spray is oriented at an angle of 62.5° relative to the XZ plane. The engine was modified for dual-fuel operation: diesel is directly injected into the cylinder, while ammonia and methanol are premixed and introduced via the intake manifold [7]. In this study, the engine operates at a typical medium load point (50% load), with an engine speed of 910 rpm and a brake mean effective pressure (BMEP) of 0.81 MPa.

The fuel energy definitions are as follows: AEF is the percentage of total energy contributed by ammonia. The pilot diesel energy remains constant throughout the study, accounting for 10% of the total energy input. Consequently, the premixed fuel (ammonia and methanol) contributes the remaining 90%. MEFP (Methanol Energy Fraction in Premixed fuel) is defined as the percentage of energy contributed by methanol relative to the total energy of the premixed fuel (ammonia + methanol). To provide a clear comparison of the fuel characteristics, the key physicochemical properties of the diesel surrogate, ammonia, and methanol used in this study are summarized in Table 2.

Table 3
The sub-model used in the simulation.

Phenomenon	Model
Combustion	SAGE
Turbulence	RNG k–ε model
Spray breakup	Hybrid KH-RT
Droplet collision	NTC collision method
Spray wall interaction	O'Rourke

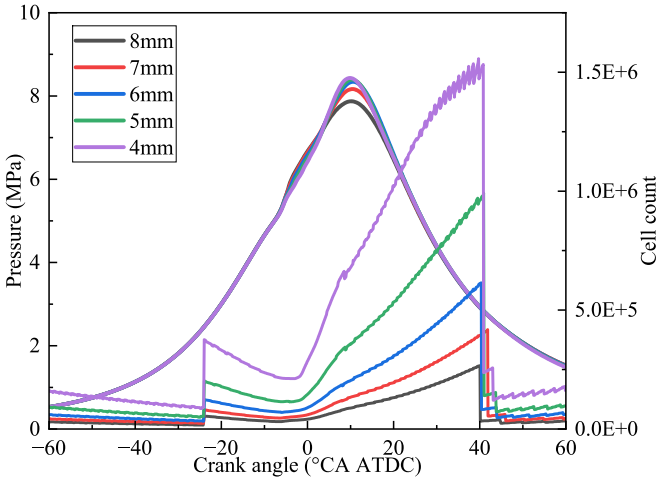

Fig. 1. Grid independence verification. Comparisons of in-cylinder pressure (left axis) and cell count (right axis) under different base grid sizes. The 5 mm grid was selected for this study to balance computational accuracy and efficiency.

2.2. Numerical simulation model

To analyze the effect of MEFP on the combustion and emissions of ammonia/diesel dual fuel engine at high AEF, the numerical study was conducted on Converge v3.0 software [28]. The sub-models are detailed in Table 3. To accurately simulate the spray and vaporization processes, tetradecane ($C_{14}H_{30}$) was employed as the physical surrogate for diesel due to their similar macroscopic properties. Meanwhile, n-heptane was utilized as the chemical surrogate to closely match the cetane number and auto-ignition delay of actual diesel fuel. A reduced n-heptane/ammonia mechanism (69 species, 389 reactions) was employed [29] coupled with the SAGE solver for combustion kinetics [30]. It should be noted that this mechanism inherently includes a comprehensive methanol sub-mechanism, enabling it to accurately capture the oxidation pathways, reaction kinetics, and cross-reactions of methanol alongside ammonia and the diesel surrogate. The in-cylinder flow was simulated by Reynolds-averaged Navier-stokes (RANS) based renormalization group k–ε model [31]. The spray and breakup of diesel were simulated by Kelvin-Helmholtz/Rayleigh-Taylor (KH-RT) model [32]. In this specific implementation, the KH mechanism simulates the primary aerodynamic stripping within the characteristic breakup length (Levich length). Beyond this distance, a competitive coupling between the KH and RT mechanisms is applied for secondary breakup, where the mechanism predicting a shorter breakup time dictates the droplet

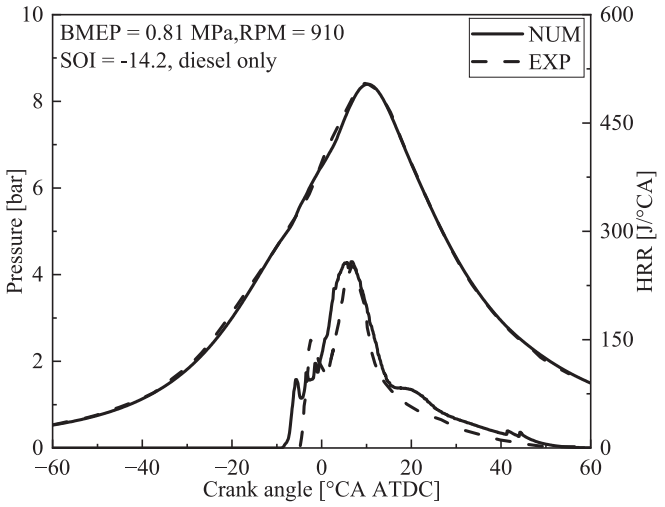

Fig. 2. Comparison of calculated in-cylinder pressure and HRR with experimental data at 100% diesel.

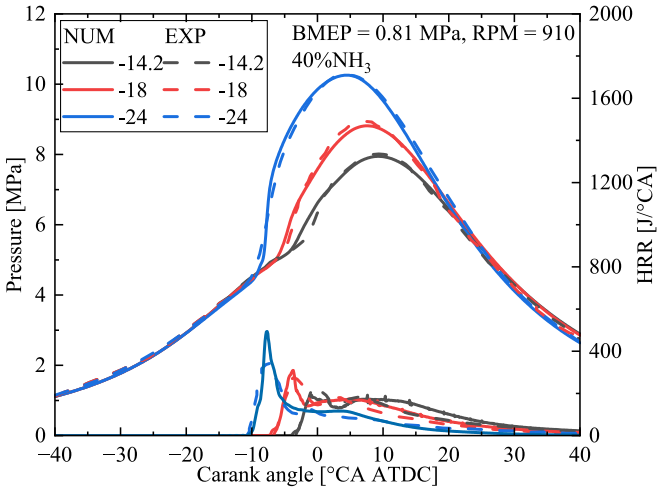

Fig. 3. Comparison of calculated in-cylinder pressure and HRR with experimental data at an AEF of 40%.

destruction. The droplet collision and spray wall interaction were simulated by no-time-counter (NTC) collision model [33] and O'Rourke model [34]. Since the simulation starts from Intake Valve Closing (IVC), the cooling effect of high latent heat of methanol was accounted for by adjusting the initial in-cylinder temperature at IVC. The initial temperature was calculated based on the energy conservation of the mixture vaporization process in the intake manifold.

2.3. Model validation

To ensure the simulation results were independent of mesh density, a grid sensitivity analysis was performed by varying the base grid size from 8 mm to 4 mm, as illustrated in Fig. 1. The in-cylinder pressure traces and total mesh cell counts were compared across these cases. As observed, the pressure profiles for the 5 mm and 4 mm grids were nearly identical, with a negligible deviation of only 0.45% in the predicted peak cylinder pressure, indicating that the solution had achieved convergence. However, the 4 mm grid resulted in a drastic increase in the total cell count (reaching approximately 1.56 million cells) compared to the 5 mm case (approximately 0.99 million cells). This roughly 1.57-fold increase leads to excessive computational cost without yielding a noticeable improvement in accuracy. Consequently, a base

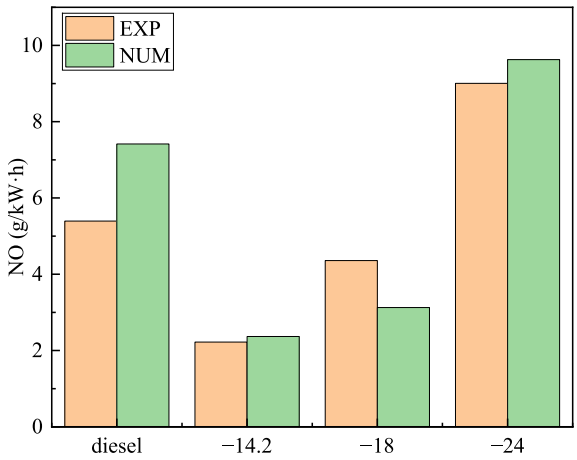

Fig. 4. Comparison of calculated NO emissions with experimental data at different AEFs and SOIs.

grid size of 5 mm was selected as the optimal compromise between calculation accuracy and efficiency. The model was validated against experimental data [7,27] under various operating conditions (Figs. 2–4). To rigorously quantify the model's accuracy, the Root Mean Square Error (RMSE) was calculated for the cylinder pressure traces. For the baseline diesel operation (Fig. 2), the pressure RMSE is exceptionally low at 0.066 MPa. Under the 40% AEF conditions (Fig. 3), the pressure RMSEs are 0.137, 0.134, and 0.179 MPa for the SOIs of −14.2, −18, and −24 °CA ATDC, respectively. Given that the peak pressures range from 8.0 to 10.3 MPa, the maximum pressure prediction error represents a relative deviation of less than 2%. Overall, the predicted in-cylinder pressure and heat release rate (HRR) showed excellent agreement with experiments. Although a slight deviation in NO emissions was observed at early SOI conditions—a common challenge in RANS-based simulations due to the sensitivity of the Zeldovich mechanism to local temperature fluctuations—the model correctly captured the emission trends and magnitude. Thus, the model is deemed robust for the qualitative and mechanistic analysis of this study.

It should be noted that while the model validation was performed at an AEF of 40% due to the safety limits of the experimental bench, the chemical kinetic mechanism employed has been widely validated under ammonia-rich conditions in previous literature [29]. Although quantitative deviations may exist at 90% AEF, the model robustly captures the qualitative trends of thermal quenching and radical competition. Since this study focuses on decoupling the governing mechanisms rather than absolute quantitative calibration, the current validation is deemed sufficient for elucidating the “tipping point” behavior of methanol.

3. Results and discussion

3.1. Baseline combustion characteristics under different AEFs

Figs. 5 and 6 illustrate the baseline effect of AEF on combustion. As AEF increases, both in-cylinder pressure and HRR decrease. Notably, when AEF exceeds 80%, the combustion phase (CA90) is severely delayed, leading to intensified post-combustion and a decline in indicated thermal efficiency (ITE). An AEF of 95% results in misfire-like conditions. Consequently, a high AEF of 90% was selected for the subsequent methanol addition study to represent a challenging operating condition that requires optimization.

Consequently, an AEF of 90% represents a critical operating boundary where the dual-fuel engine suffers from severe performance degradation. This specific condition was therefore selected as the focal point for the subsequent investigation, aiming to explore whether methanol addition can recover combustion stability and efficiency.

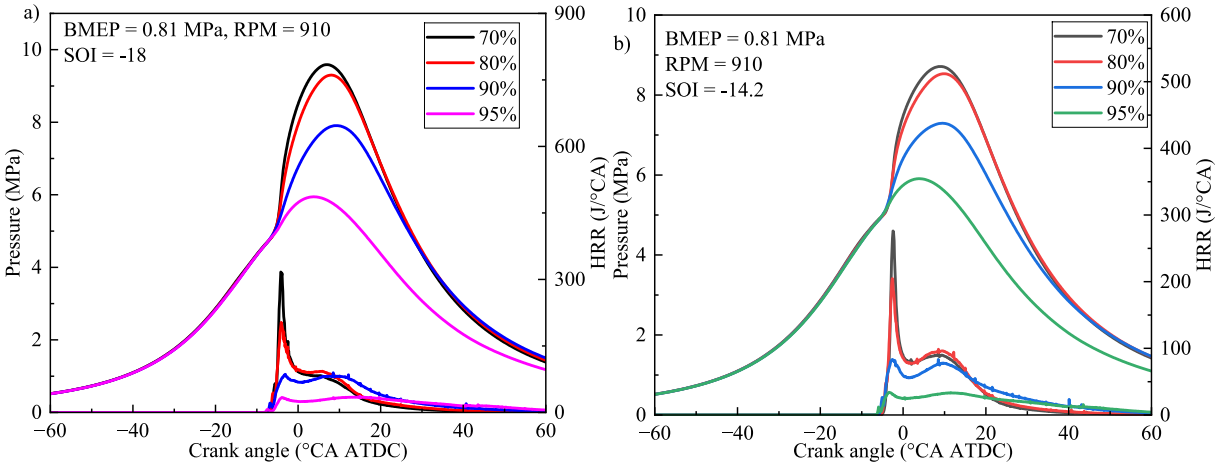

Fig. 5. Effect of AEF on the in-cylinder pressure and HRR at SOIs of −18 and −14.2 °CA ATDC.

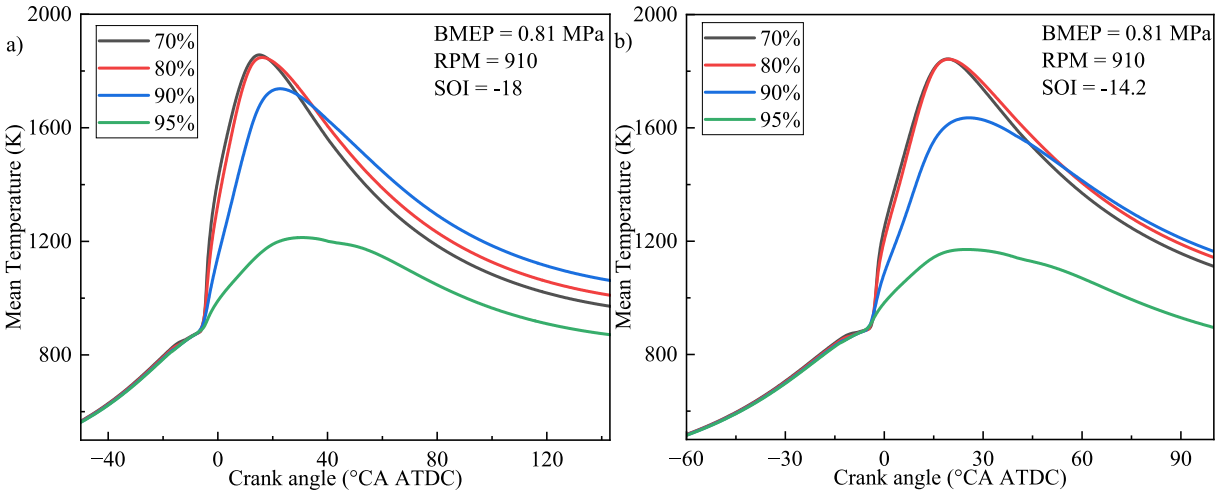

Fig. 6. Effect of AEF on mean in-cylinder temperature at SOIs of −18 and −14.2 °CA ATDC.

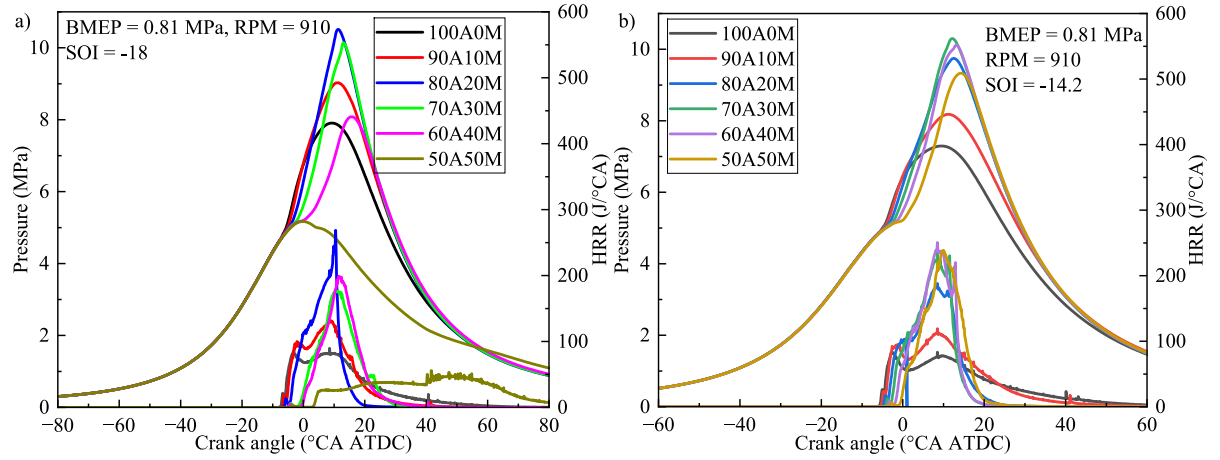

Fig. 7. Effect of MEFP on in-cylinder pressure and HRR at SOIs of −18 and −14.2 °CA ATDC.

3.2. Impact of Methanol Energy Fraction on Combustion and Emissions

Fig. 7 illustrates the in-cylinder pressure and HRR profiles. At an early SOI (−18 °CA ATDC, Fig. 7a)), the combustion exhibits a non-monotonic response. Initially, as MEFP increases from 0% to 30%, the peak pressure and HRR rise, indicating that the chemical reactivity of methanol promotes combustion. However, when MEFP reaches 50%, the combustion deteriorates sharply, with peak pressure collapsing below the baseline. This phenomenon is mechanistically explained by Fig. 8, which depicts the mean in-cylinder temperature. At an SOI of

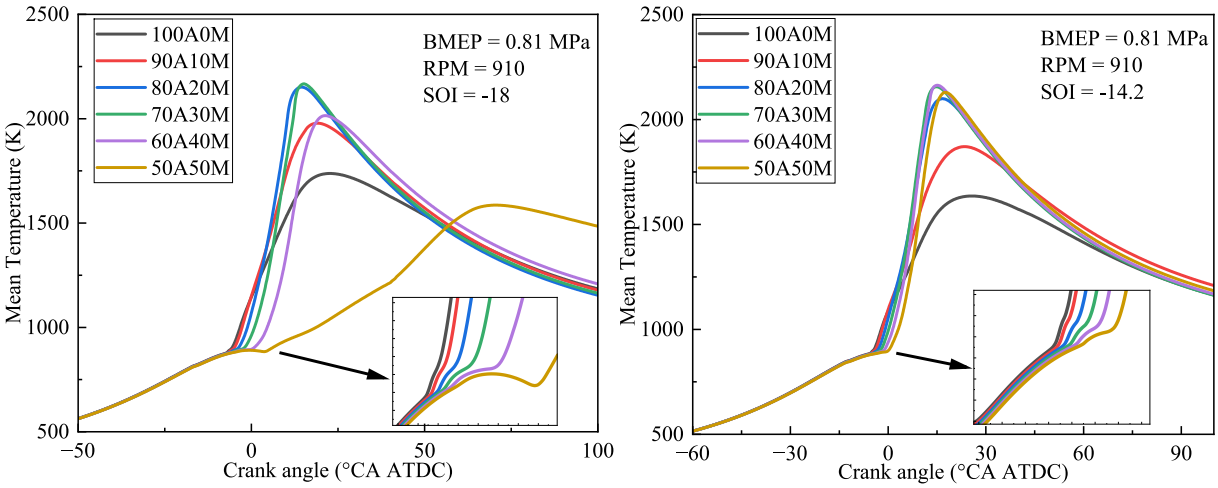

Fig. 8. Effect of MEFP on mean in-cylinder temperature at SOIs of −18 and −14.2 °CA ATDC.

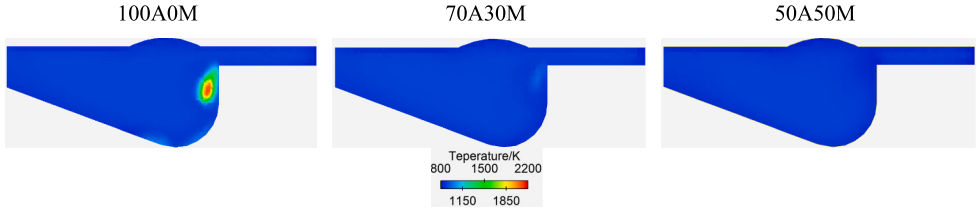

Fig. 9. Local temperature distribution contours near the diesel spray plumes at the ignition timing for 0%, 30%, and 50% MEFP (SOI = −18 °CA ATDC).

−18 °CA ATDC, the addition of high-fraction methanol (50%) causes a significant reduction in the temperature during the compression stroke due to methanol's high latent heat of vaporization. As shown in Fig. 8 b), the peak temperature at 50% MEFP is not only significantly lower but also delayed to 60 °CA ATDC (post combustion stage). This strong thermal quenching effect significantly reduces the local temperature of the pilot fuel, inhibiting the auto-ignition of the diesel droplets. Similar phenomena have been reported in previous studies [35,36], where the excessive charge cooling caused by the high latent heat of alcohol fuels (methanol or ethanol) was identified as a primary driver for partial combustion or misfire in dual-fuel engines. Leading to the observed combustion failure in the current study.

In contrast, at a late SOI (−14.2 °CA ATDC, Fig. 7b)), the cylinder environment is hotter and denser at the time of injection. Consequently, Fig. 8b) shows that even at 50% MEFP, the mean in-cylinder temperature remains robust, without the collapse observed in the early SOI case. This suggests that retarding the SOI effectively compensates for the cooling effect of methanol, allowing its chemical promoting effect to dominate.

While the mean in-cylinder temperature provides a global thermodynamic perspective, the auto-ignition of the diesel pilot relies heavily on the local thermal environment. To provide direct spatial evidence for the physical mechanisms behind the ignition failure at high MEFPs, Fig. 9 presents the local temperature distribution contours near the diesel spray plumes at the ignition timing for the early SOI (−18 °CA ATDC) strategy.

As illustrated, the local high-temperature ignition kernels exhibit a progressive deterioration with the increase of methanol fraction. At the baseline 0% MEFP, a highly distinct and intense high-temperature ignition kernel (characterized by the prominent red regions) is

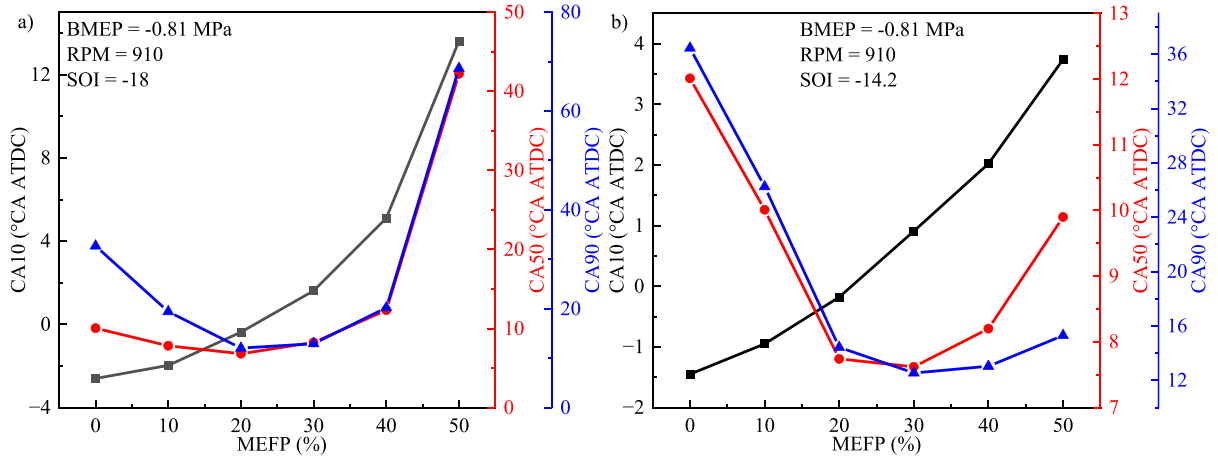

Fig. 10. The effect of MEFP on CA10, CA50, and CA90 at SOIs of −18 and −14.2 °CA ATDC.

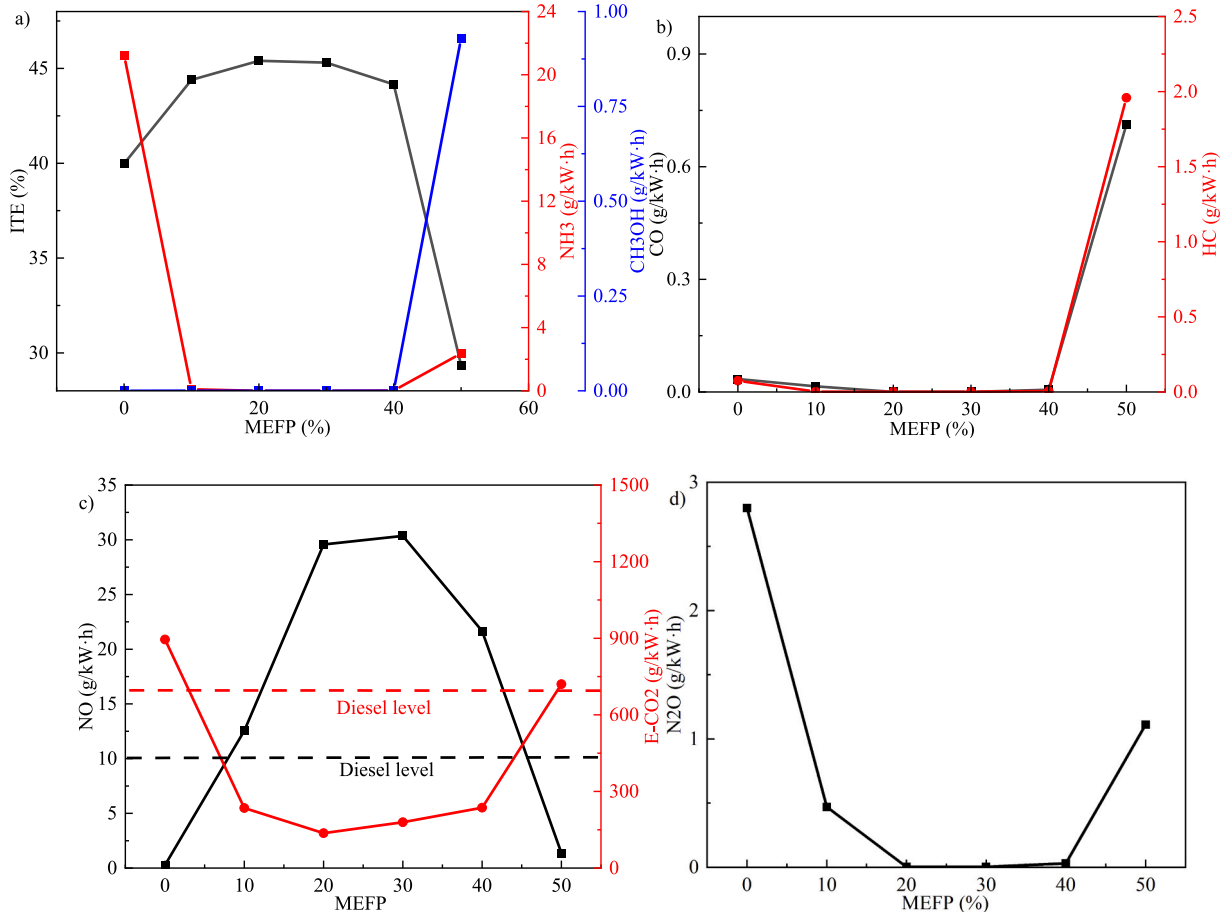

Fig. 11. Effect of MEFP on ITE and emissions at an SOI of −18 °CA ATDC (The Equivalent CO_2 (*E*-CO_2) was calculated using the Global Warming Potential (GWP) values over a 100-year horizon: $CO_2 = 1$, $N_2O = 298$, and unburned $NH_3 = 0$ (assuming eventual deposition or oxidation in the atmosphere, though its indirect GWP is noted).)

successfully established at the spray periphery. When MEFP increases to 30%, although auto-ignition still occurs, the peak temperature of the local ignition kernel is noticeably suppressed by the cooling effect of methanol, appearing only slightly hotter than the surrounding mixture. Finally, when the MEFP reaches the critical threshold of 50%, a stark macroscopic transformation is observed. The massive vaporization of methanol absorbs substantial heat, drastically reducing the local temperatures, and the local high-temperature regions almost completely vanish (evidenced by the widespread blue and green low-temperature regions). This direct visual evidence confirms that the physical thermal quenching acts as a progressive and dominant trigger; it effectively freezes the local thermal environment, prevents early kernel development, and ultimately leads to the global combustion deterioration and massive unburned fuel slip discussed previously.

Fig. 10 presents the combustion phasing (CA10, CA50, CA90). Generally, CA10 is delayed with increasing MEFP due to the cooling-induced ignition delay. However, the impact on CA50 and CA90 differs by SOI. At −18 °CA ATDC, CA90 is severely prolonged when MEFP exceeds 40%, confirming the unstable late-stage combustion. At −14.2 °CA ATDC, the phasing remains relatively stable even at high MEFPs, further verifying the robustness of the late injection strategy.

The trade-off between efficiency and emissions is analyzed in Fig. 10 (Early SOI) and Fig. 11 (Late SOI). For the early SOI case (−18 °CA ATDC):

1) ITE, NH_3 and CH_3OH (Fig. 11 a)): ITE improves initially (peaking at 45.4% at 20% MEFP) but plummets by 29.3% when MEFP reaches 50%. Correspondingly, the emissions of unburned NH_3 and CH_3OH, which are effectively suppressed at low MEFPs, surge to 2.369 g/kWh and 0.93 g/kWh at 50% MEFP due to the aforementioned misfire-like conditions.
2) CO and HC (Fig. 11 b)): Under stable combustion (0–40% MEFP), CO and HC emissions decrease as MEFP increases, approaching zero. However, at the tipping point of 50% MEFP, both CO and HC spike sharply, serving as further evidence of incomplete oxidation caused by thermal quenching.
3) NO and *E*-CO_2 (Fig. 11 c)): NO emissions exhibit a "bell-shaped" trend, peaking at 20–30% MEFP (reaching ~3 times the diesel level) before dropping at 50%. This peak is attributed to the enhanced flame speed of methanol creating local high-temperature zones. E-CO_2 (Equivalent CO_2) follows a trend similar to efficiency but is highest at 50% MEFP due to the severe greenhouse gas impact of unburned fuel species.
4) NO and N_2O trade-off (Fig. 11 d)): A profound trade-off relationship between NO and N_2O emissions is explicitly captured, which is fundamentally governed by the in-cylinder temperature variations. At 0% MEFP, the relatively lower bulk temperature results in low NO but high N_2O emissions (2.80 g/kWh). As MEFP increases to 20–30%, the enhanced combustion yields higher local temperatures (>1500 K), which promote thermal NO formation while effectively destroying N_2O (dropping below 0.003 g/kWh). However, at 50% MEFP, the severe thermal quenching induced by high latent heat of methanol drastically reduces the bulk temperature. This cooling effect completely suppresses NO formation but shifts the thermal environment back into the intermediate temperature window

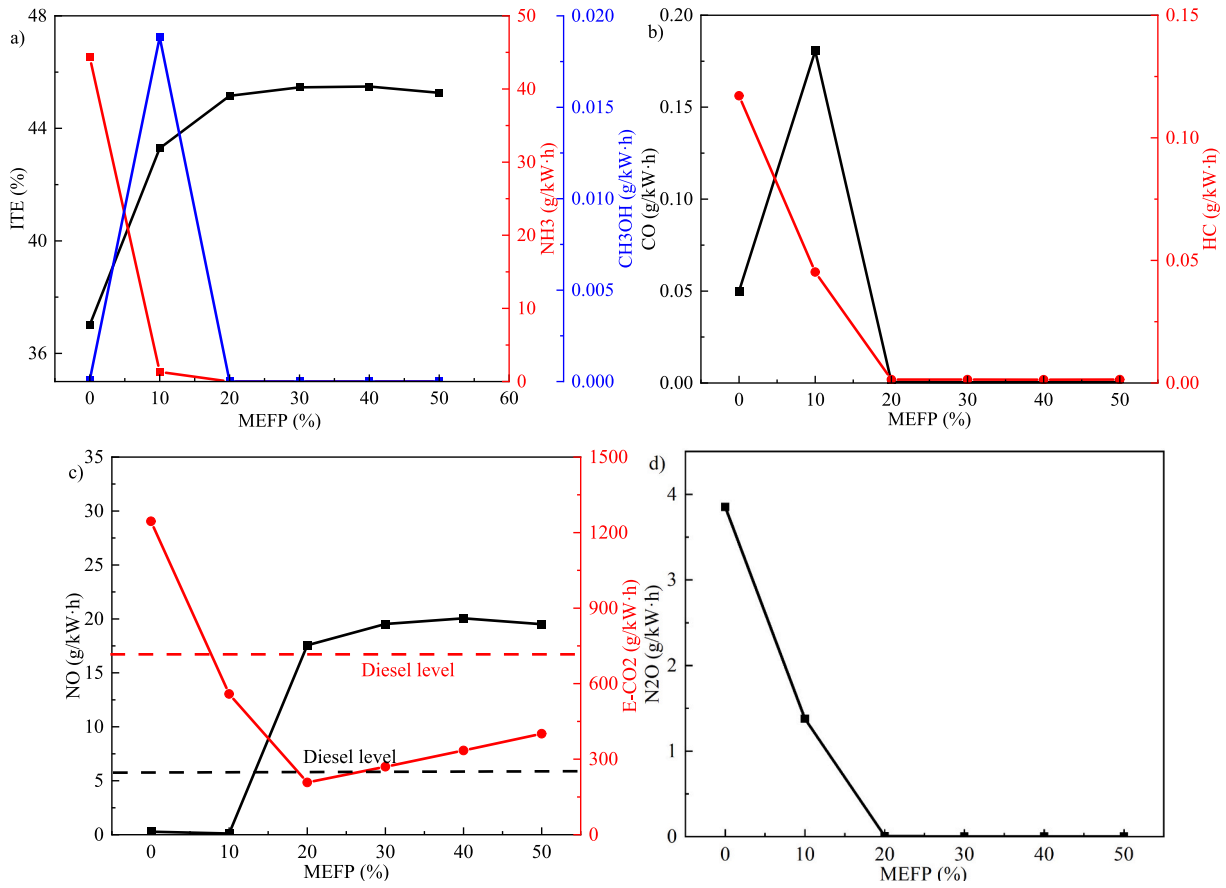

Fig. 12. Effect of MEFP on ITE and emissions at an SOI of −14.2 °CA ATDC.

(approximately 1100–1400 K), causing a sharp rebound in N_2O emissions to 1.11 g/kWh.

For the late SOI case (−14.2 °CA ATDC), the trends are distinct:

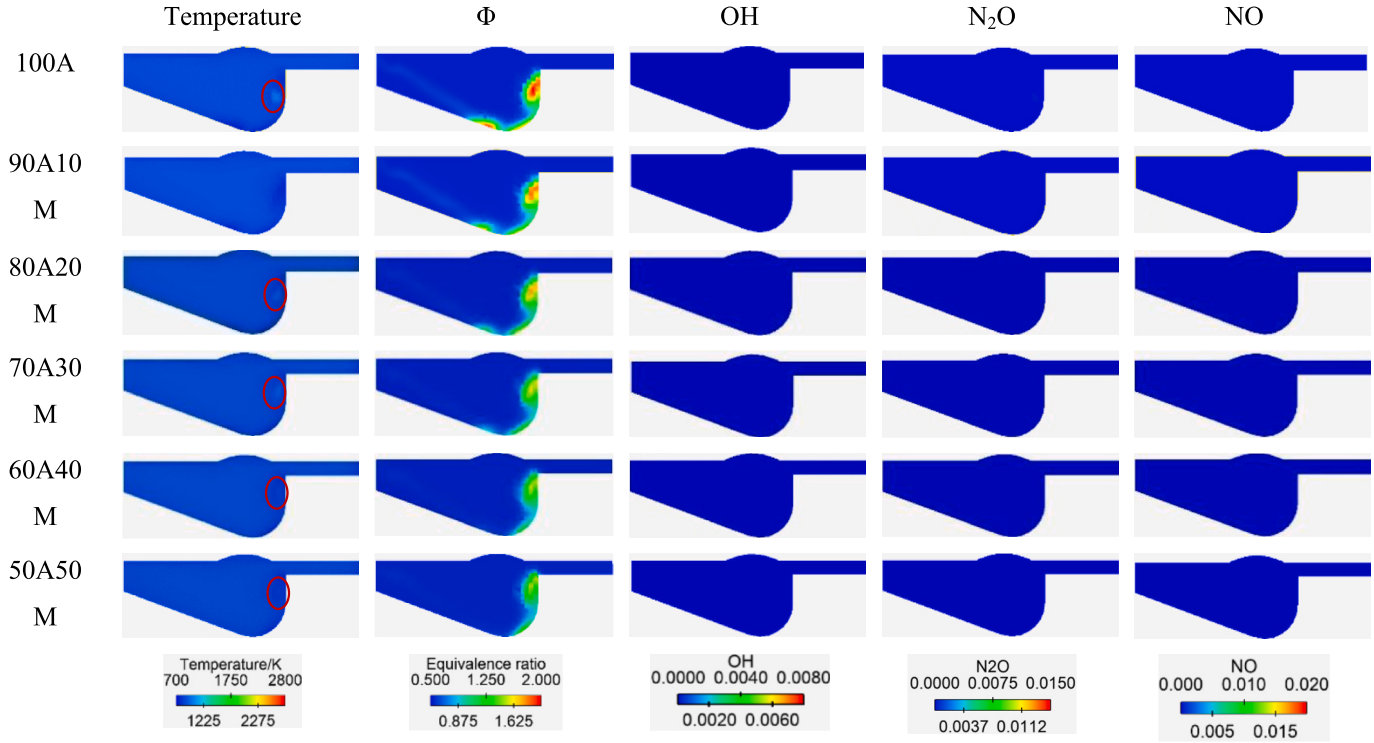

Fig. 13. Effect of MEFP on the distributions of temperature, equivalence ratio, OH, N_2O and NO at an SOI of −18 °CA ATDC and IT.

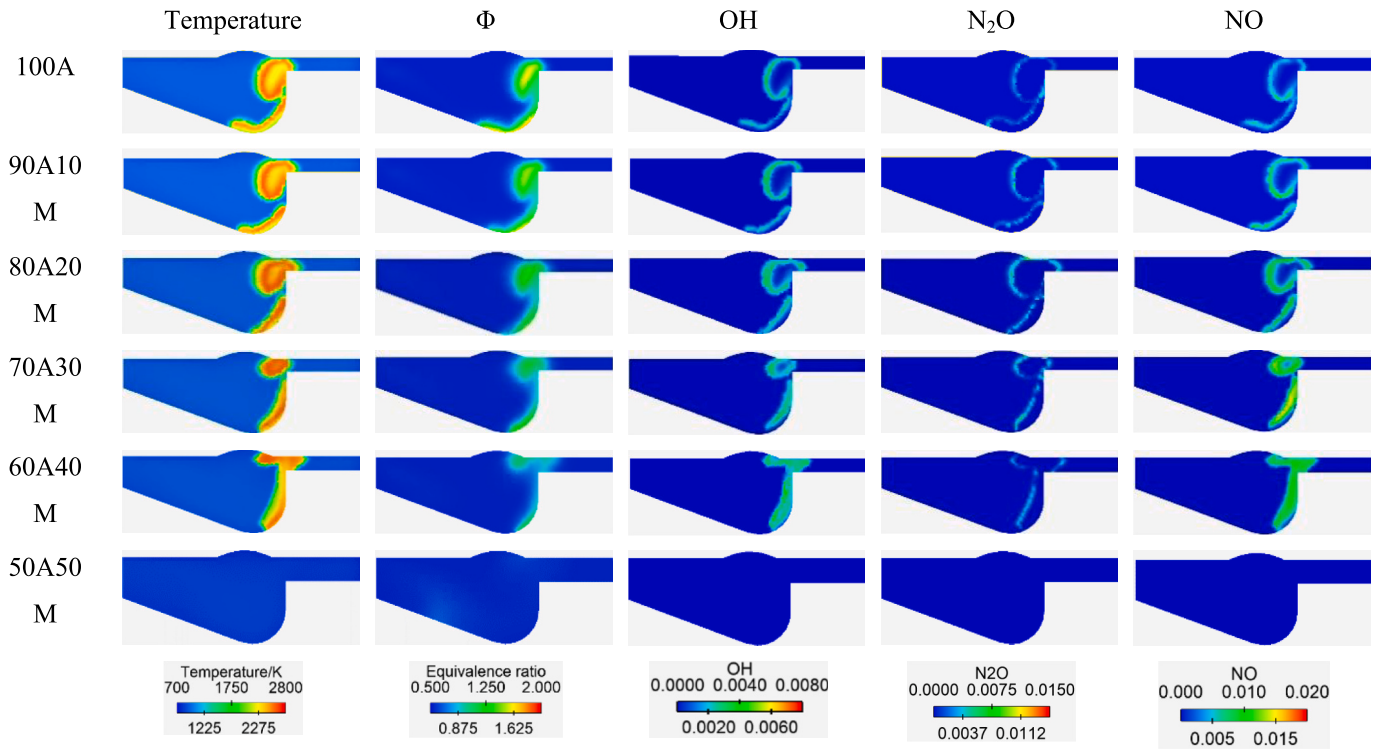

Fig. 14. Effect of MEFP on the distributions of temperature, equivalence ratio, OH, N_2O and NO at an SOI of −18 °CA ATDC and CA10.

1) ITE, NH_3 and CH_3OH (Fig. 12 a)): This strategy identifies an optimal operating window. Increasing MEFP from 0% to 10% boosts ITE from 37.0% to 43.3% (a relative improvement of 17.0%) while achieving a dramatic 97% reduction in NH_3 emissions, with the CH_3OH emissions also maintained at extremely low levels (0.0188). Unlike the early SOI case, ITE remains stable even at higher MEFPs.

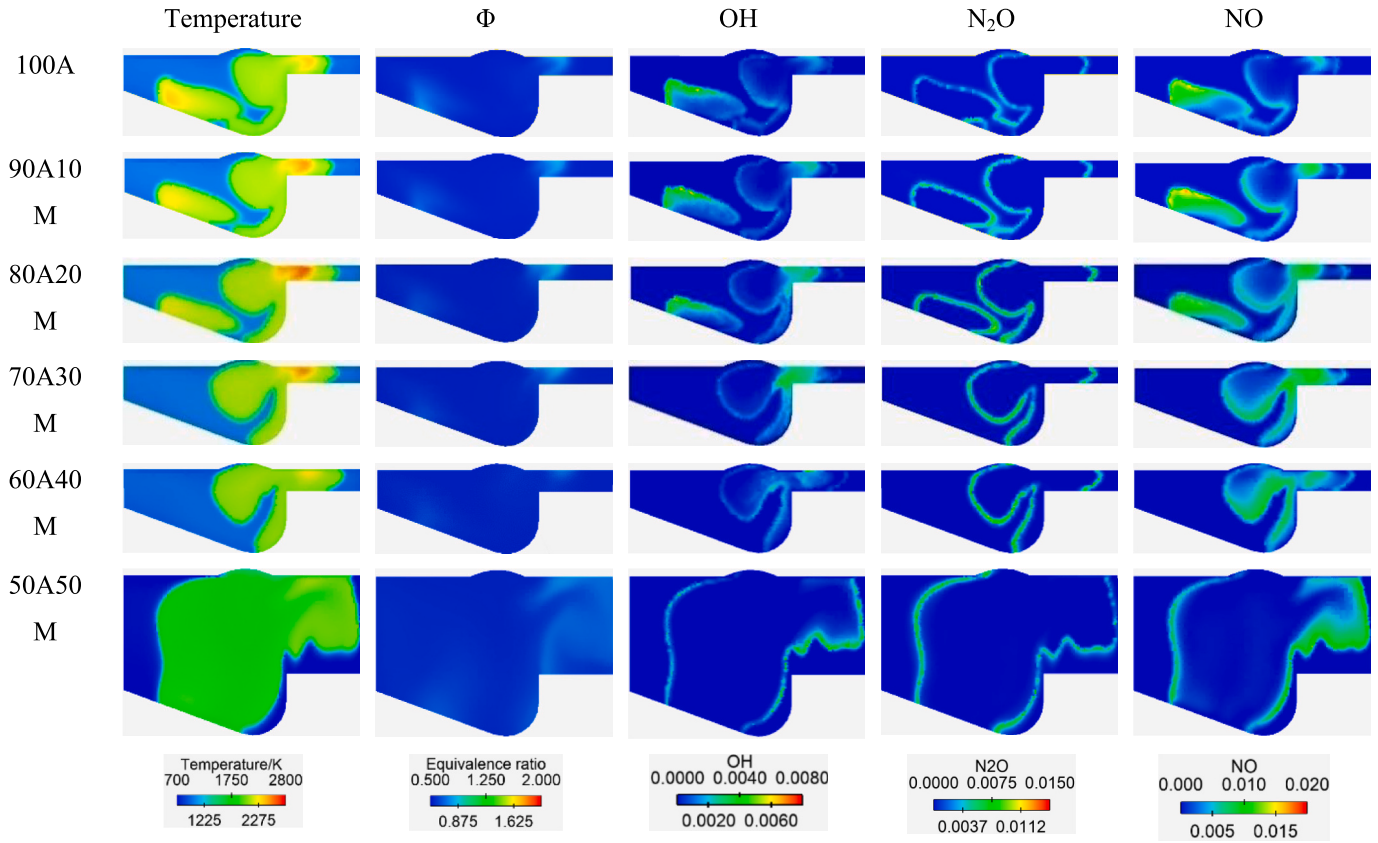

Fig. 15. Effect of MEFP on the distributions of temperature, equivalence ratio, OH, N_2O and NO at an SOI of −18 °CA ATDC and CA50.

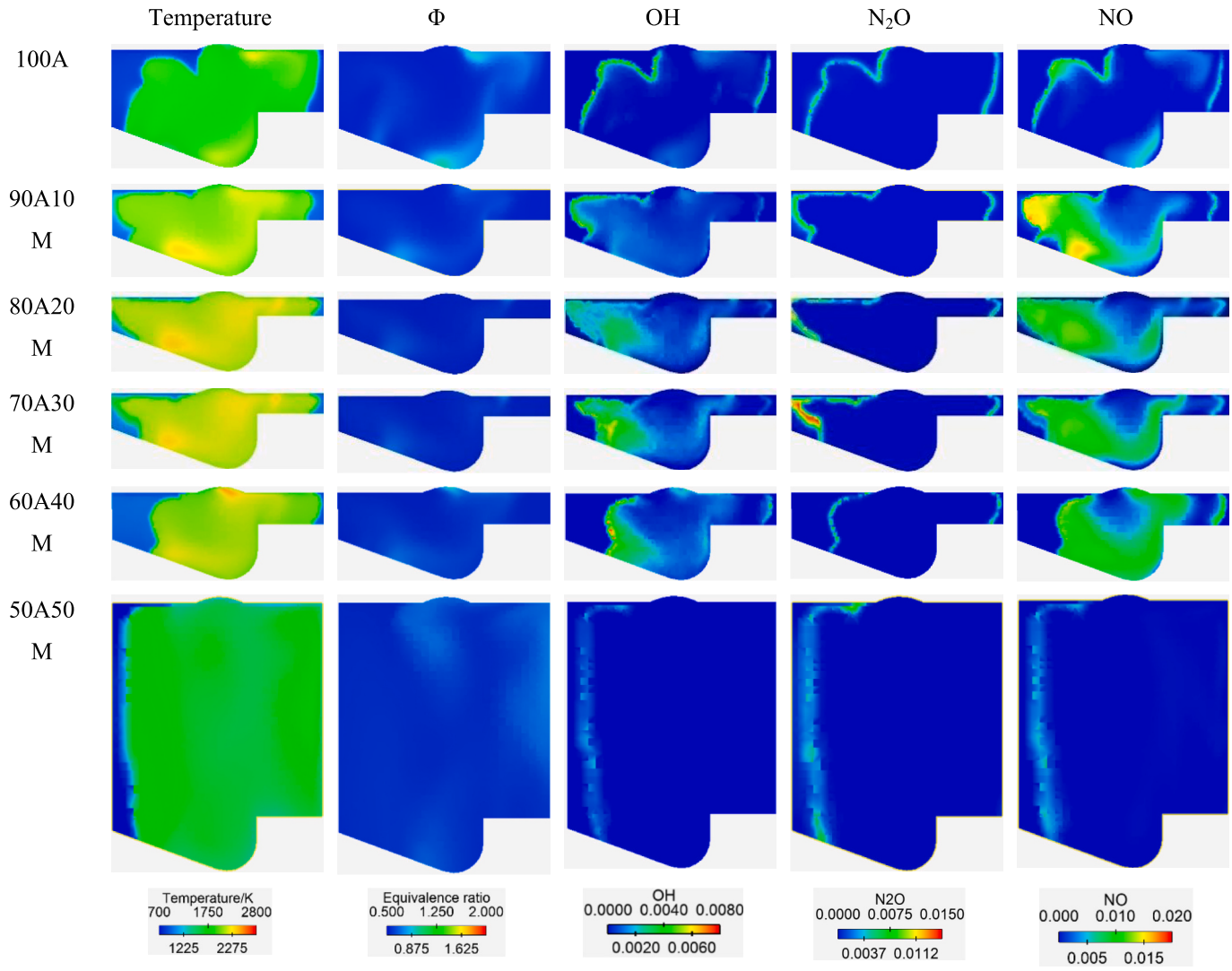

Fig. 16. Effect of MEFP on the distributions of temperature, equivalence ratio, OH, N_2O and NO at an SOI of −18 °CA ATDC and CA90.

2) CO and HC (Fig. 12 b)): Both CO and HC emissions are maintained at extremely low levels across the entire MEFP sweep. A minor increase in CO is observed at 10% MEFP, likely due to slight methanol slip, but it is rapidly oxidized at higher blends.
3) NO and *E*-CO_2 (Fig. 12 c)): A significant advantage of this strategy is observed at 10% MEFP, where NO emissions remain near zero. However, a trade-off exists: increasing MEFP beyond 20% causes NO to rise sharply. Consequently, the combination of SOI –14.2 °CA ATDC and 10% MEFP is identified as the optimal "sweet spot," simultaneously achieving high efficiency, near-zero NH_3, and ultra-low NO emissions.
4) NO and N_2O trade-off (Fig. 12 d)): The late SOI strategy exhibits a distinct NO-N_2O trade-off trajectory. At 0% MEFP, N_2O emission is prominent (3.85 g/kWh). At the optimal 10% MEFP, a favorable balance is achieved where NO remains near zero and N_2O is substantially reduced to 1.38 g/kWh. Further increasing MEFP (20–50%) enhances the local combustion temperatures and flame speeds, which strongly promotes the high-temperature thermal NO pathways. Consequently, NO emissions rise sharply, while N_2O is effectively consumed and diminished to near-zero levels (<0.007 g/kWh). This trade-off further solidifies that the combination of SOI –14.2 °CA ATDC and 10% MEFP provides the optimal compromise for mitigating the comprehensive greenhouse gas footprint.

In summary, the macroscopic results verify that retarding the SOI is a prerequisite for unlocking the benefits of methanol. The combination of a late SOI (−14.2 °CA ATDC) with a moderate MEFP (10%) effectively breaks the trade-off between efficiency and emissions, emerging as the optimal configuration for medium-load operation.

3.3. Mechanism Analysis of Spatial Distributions

To reveal the fundamental chemical kinetics driving the macroscopic performance observed in Section 3.2, the spatial evolution of temperature, equivalence ratio (Φ), and critical species (OH, NO, N_2O) was analyzed. The distributions are examined at four key moments: Ignition Timing (IT), CA10, CA50, and CA90.

3.3.1. Mechanism under early Injection Strategy (SOI = −18 °CA ATDC)

Figs. 12 to 15 depict the evolution of the in-cylinder field under the early SOI strategy. The comparison between the baseline (0% MEFP) and the high methanol case (50% MEFP) reveals the mechanism of combustion deterioration.

Ignition and Early Flame Development (IT & CA10): At IT (Fig. 13), the baseline case shows a developing high-temperature kernel. However, at 50% MEFP, the cooling effect of methanol vaporization suppresses low-temperature reactions, resulting in a significantly cooler charge. By CA10 (Fig. 14), a stark contrast emerges: while the 0–20%

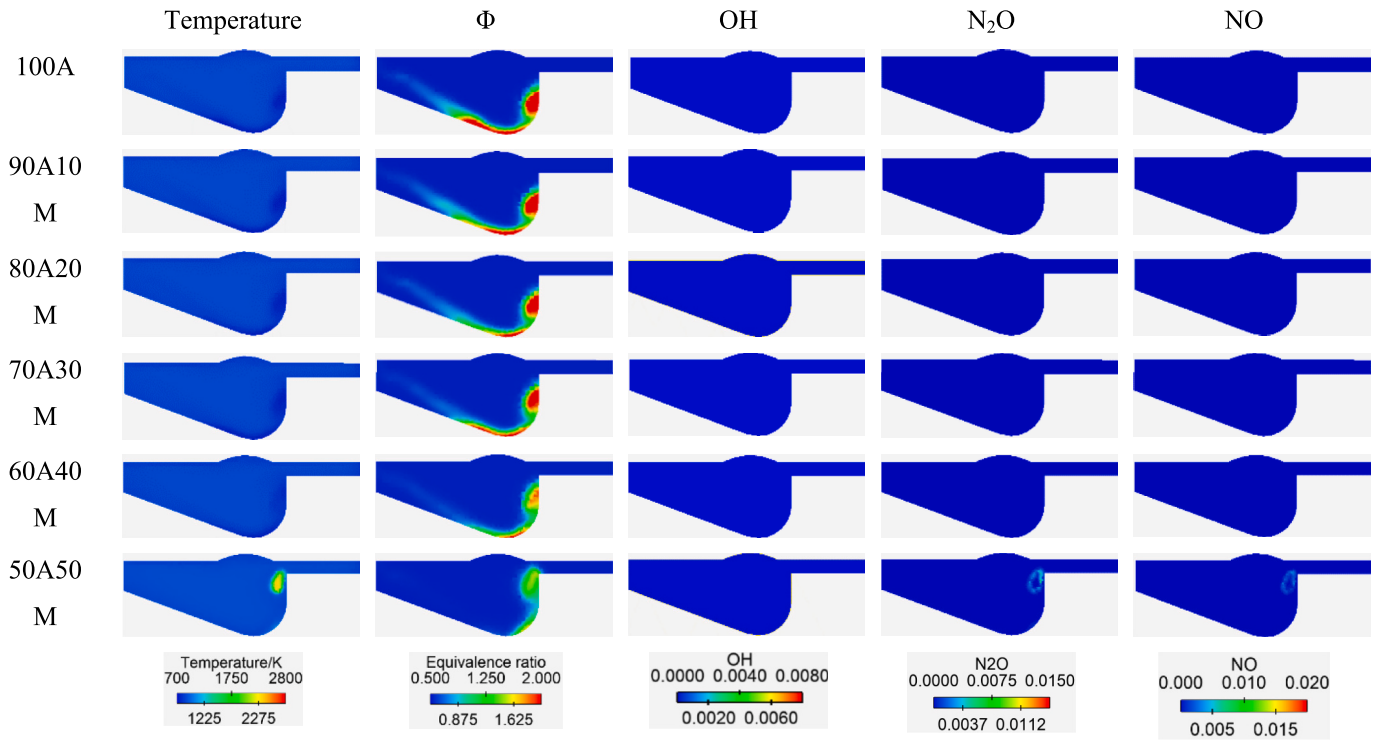

Fig. 17. Effect of MEFP on the distributions of temperature, equivalence ratio, OH, N_2O and NO at an SOI of −14.2 °CA ATDC and IT.

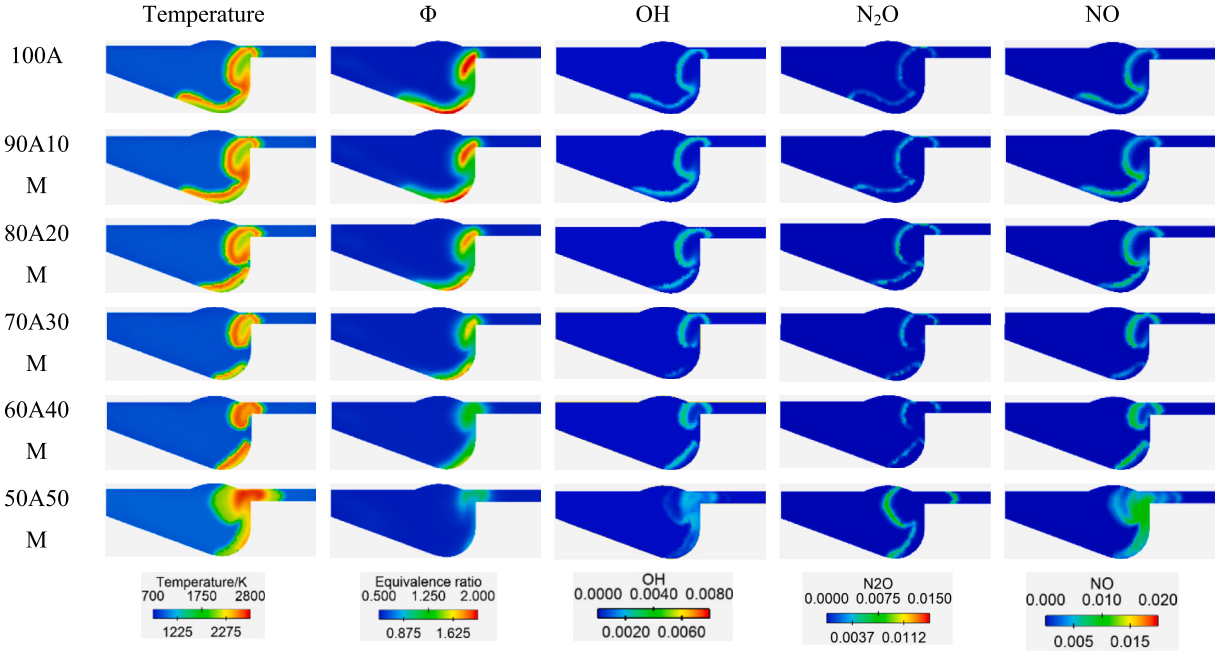

Fig. 18. Effect of MEFP on the distributions of temperature, equivalence ratio, OH, N_2O and NO at an SOI of −14.2 °CA ATDC and CA10.

MEFP cases exhibit a robust high-temperature core (>2000 K) with abundant OH radicals, the 50% MEFP case shows almost no distinct high-temperature region. The OH radicals, which are essential for oxidizing NH_3, are virtually absent. This explains the delayed ignition and initial heat release lag observed in Fig. 7a).

Main Combustion Phase (CA50–Fig. 15): As combustion progresses to CA50, the impact of thermal quenching becomes critical. For low MEFPs, OH radicals are distributed throughout the high-temperature regions, and NO is formed in these overlapping high-T/high-OH zones via the thermal mechanism. Conversely, at 50% MEFP, the high-temperature region is "smeared" and uniform but remains at a low level (~1800 K). Crucially, OH radicals are confined strictly to the periphery. This severe spatial disconnect, quantified by the minimal overlap between fuel-rich zones (high Φ) and the oxidizer pool (OH radicals), inhibits the complete oxidation of ammonia, directly leading to the high unburned NH_3 emissions of ammonia, directly leading to the high unburned NH_3 emissions reported in Fig. 10.

Late Combustion Phase (CA90– Fig. 16): At the final stage, the 50% MEFP case still fails to establish a robust flame. The N_2O distribution provides key insight: N_2O is primarily found at the edges of the OH/NO

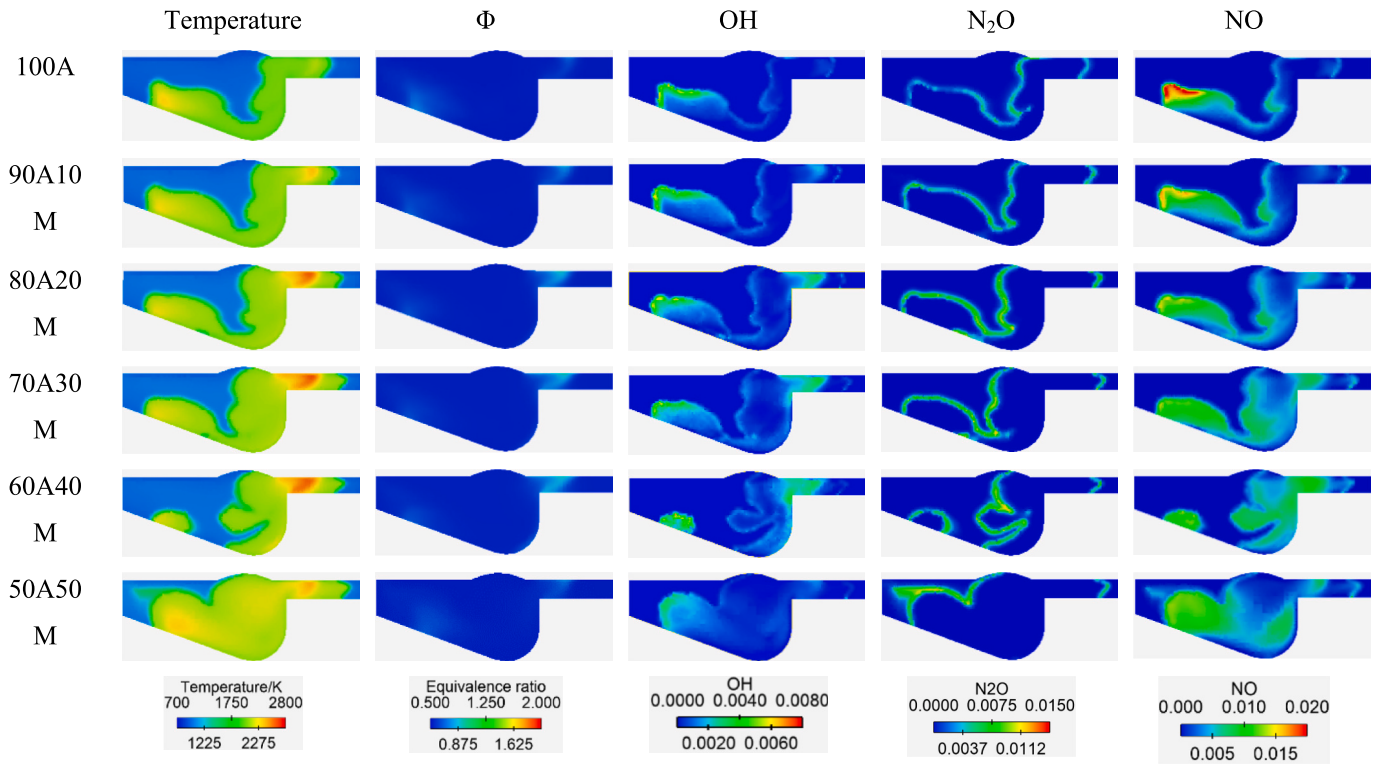

Fig. 19. Effect of MEFP on the distributions of temperature, equivalence ratio, OH, N_2O and NO at an SOI of −14.2 °CA ATDC and CA50.

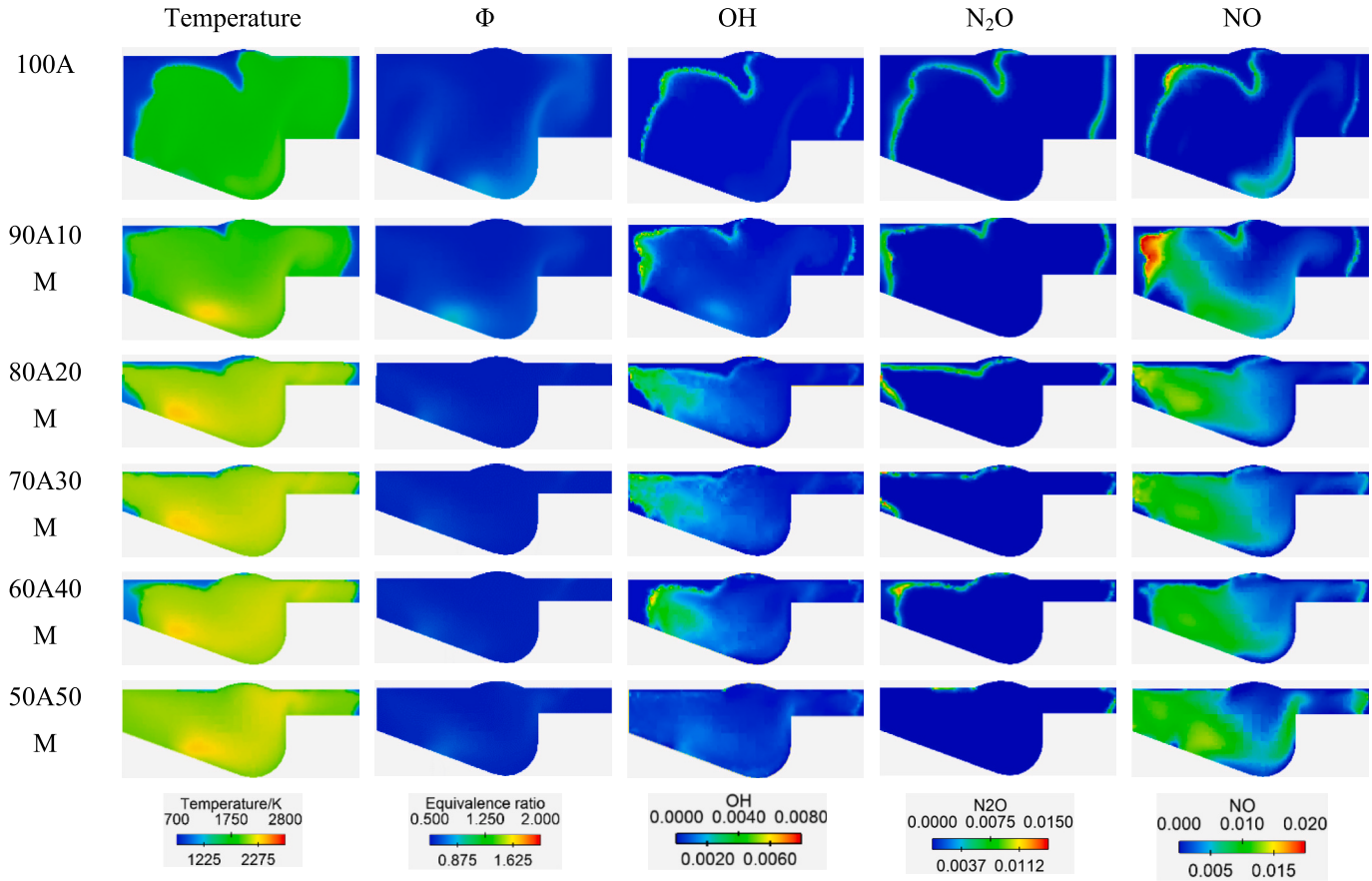

Fig. 20. Effect of MEFP on the distributions of temperature, equivalence ratio, OH, N_2O and NO at an SOI of −14.2 °CA ATDC and CA90.

regions. In successful combustion (low MEFP), this N_2O is an intermediate that is eventually consumed. However, in the quenched combustion of 50% MEFP, the reaction path is truncated, allowing N_2O and NH_3 to survive into the exhaust.

3.3.2. Mechanism under late Injection Strategy (SOI = −14.2 °CA ATDC)

Figs. 17 to 20 illustrate the process under the late SOI strategy, explaining why this strategy successfully accommodates methanol.

Ignition Robustness (IT & CA10): Unlike the early SOI case, the late injection occurs in a hotter, more compressed environment. At IT (Fig. 17) and CA10 (Fig. 18), even with 50% methanol, a local high-temperature region is successfully established downstream of the fuel jet. The diesel pilot acts as a robust "radical seed," generating an initial pool of OH radicals that withstands the cooling effect of methanol.

Flame Propagation (CA50 – Fig. 19): The synergy between diesel and methanol becomes evident here. As MEFP increases, the OH radical distribution extends from the pilot flame into the premixed ammonia/methanol zone. Methanol, with its lower C-H bond energy compared to ammonia, decomposes rapidly to replenish the OH pool. This sustainable radical propagation ensures that the equivalence ratio (Φ) decreases efficiently toward 1.0 (stoichiometric), indicating complete fuel consumption.

Pollutant Formation Mechanism (CA90 – Fig. 20): The spatial overlap of species at CA90 elucidates the emissions trade-off. NO is strictly confined to the highest temperature cores where OH concentration is high. At 10% MEFP, the high-temperature region is moderate, keeping NO levels low. However, as MEFP increases, the high-temperature zone expands (due to methanol's faster burning velocity), causing the NO region to grow. Meanwhile, N_2O remains wrapped around the outer periphery of the NO cloud. The late SOI strategy ensures that the in-cylinder temperature is high enough to consume N_2O and NH_3, but—at the optimal 10% MEFP point—not high enough to trigger massive thermal NO formation, thus achieving the "sweet spot" identified in Fig. 12.

Collectively, these spatial evolutions reveal the governing mechanism: the macroscopic performance deterioration at early SOI is fundamentally driven by the thermal quenching of the OH radical pool, whereas the late SOI strategy succeeds by utilizing the higher ambient temperature to sustain a radical-rich environment, thereby ensuring complete oxidation pathways.

4. Conclusion

This study performed a comprehensive numerical investigation into the coupling effects of injection strategy and methanol blending, identifying an optimal configuration (SOI = −14.2 °CA ATDC, 10% MEFP) that achieves a diesel-like thermal efficiency of 43.3% with a 97% reduction in unburned NH_3. By focusing on a high ammonia energy fraction (90%) scenario, the work decouples the complex interactions between thermodynamic cooling and chemical reactivity enhancement. The key findings and their implications are summarized as follows:

1. Methanol does not essentially act as a combustion promoter; its role is strictly regulated by the start of injection (SOI). At an early SOI (−18 °CA ATDC), methanol exhibits a "tipping point" behavior. While low fractions (<30%) improve reactivity, exceeding a critical threshold of 40% triggers severe combustion deterioration, characterized by a 26.6% drop in thermal efficiency and a surge in unburned NH_3. This is mechanistically attributed to the thermal quenching effect, where high latent heat of methanol cools the charge below the threshold required for sustained diesel auto-ignition.
2. Retarding the injection timing to −14.2 °CA ATDC proves to be the effective strategy for mitigating methanol's cooling penalty. The higher in-cylinder temperature at this timing compensates for the latent heat absorption, allowing the chemical promoting effect of methanol (via radical supply) to dominate. This strategy significantly reduces the sensitivity of combustion phasing to methanol variations, ensuring robust operation.
3. A synergistic "sweet spot" for medium-load operation was identified. The combination of a retarded SOI (−14.2 °CA ATDC) with a 10% methanol energy fraction (MEFP) achieved an indicated thermal efficiency of 43.3%, comparable to pure diesel operation. Crucially, this configuration reduced unburned NH_3 emissions by 97% relative to the baseline and maintained NO emissions at near-zero levels, effectively resolving the efficiency-emissions trade-off inherent to ammonia engines.
4. Chemical kinetic analysis revealed that the sustainability of the OH radical pool is the governing factor for performance. Under the optimal strategy, the diesel pilot acts as a robust "radical seed" that rapidly propagates into the premixed ammonia/methanol zone. In contrast, the performance collapse at early SOI is driven by the spatial disconnect between fuel-rich regions and OH radicals, which halts the oxidation pathway of NH_3 and leads to incomplete combustion.

These findings challenge the conventional reliance on early injection for premixed combustion in ammonia engines. This study establishes a theoretical framework suggesting that for triple-fuel systems (Ammonia-Methanol-Diesel), thermal management via injection timing retardation is prerequisite to unlocking the chemical potential of reactive additives.

CRediT authorship contribution statement

Jingrui Li: Writing – review & editing, Supervision, Methodology, Investigation, Conceptualization. **Sijie He:** Writing – original draft, Investigation. **Guyu Feng:** Validation, Methodology. **Changchun Xu:** Software, Investigation. **Haifeng Liu:** Supervision, Funding acquisition. **Xinyan Wang:** Validation, Software. **Hua Zhao:** Supervision.

Declaration of competing interest

The authors declare that they have no known competing financial interests or personal relationships that could have appeared to influence the work reported in this paper.

Data availability

Data will be made available on request.

Acknowledgements

This work was supported by the National Key Research and Development Program of China (NO. 2023YFE0115300).

References

[1] C. Kurien, M. Mittal, Review on the production and utilization of green ammonia as an alternate fuel in dual-fuel compression ignition engines, Energ. Conver. Manage. 251 (2022) 114990.
[2] P.K. Senecal, F. Leach, Diversity in transportation: why a mix of propulsion technologies is the way forward for the future fleet, Results Eng. 4 (2019) 100060.
[3] H. Kou, W. Hu, T. Li, et al., Effects of injection timing on combustion and mixture formation of a methanol direct injection engine equipped with a small volume passive pre-chamber, Fuel 384 (2025) 133910.
[4] X. Yin, X. Ren, J. Wang, et al., Influence of methanol and diesel injection timings on the maximum methanol energy substitution ratio and performance of diesel/methanol dual-direct injection engine, Energy 318 (2025) 134762.
[5] P. Dimitriou, R. Javaid, A review of ammonia as a compression ignition engine fuel, Int. J. Hydrogen Energy 45 (11) (2020) 7098–7118.
[6] J. Li, X. Liu, H. Wang, et al., Kinetic study of ignition process of ammonia/n-heptane fuel blends under engine conditions, Energy Sci. Eng. 12 (3) (2024) 1091–1109.
[7] A. Yousefi, H. Guo, S. Dev, et al., Effects of ammonia energy fraction and diesel injection timing on combustion and emissions of an ammonia/diesel dual-fuel engine, Fuel 314 (2022) 122723.

[8] A.J. Reiter, S.-C. Kong, Combustion and emissions characteristics of compression-ignition engine using dual ammonia-diesel fuel, Fuel 90 (1) (2011) 87–97.
[9] J. Shin, S. Park, Numerical analysis for optimizing combustion strategy in an ammonia-diesel dual-fuel engine, Energ. Conver. Manage. 284 (2023) 116980.
[10] R. Chen, T. Li, X. Wang, et al., Engine-out emissions from an ammonia/diesel dual-fuel engine – the characteristics of nitro-compounds and GHG emissions, Fuel 362 (2024) 130740.
[11] L. Xu, S. Xu, X.-S. Bai, et al., Performance and emission characteristics of an ammonia/diesel dual-fuel marine engine, Renew. Sustain. Energy Rev. 185 (2023) 113631.
[12] S. Mi, Z. Shi, H. Wu, et al., Expanding high ammonia energy ratios in an ammonia-diesel dual-fuel engine across wide-range rotational speeds, Appl. Therm. Eng. 251 (2024) 123608.
[13] L. Chen, W. Zhao, R. Zhang, et al., Flame characteristics and abnormal combustion of ammonia-diesel dual-fuel engine with considering ammonia energy fractions, Appl. Therm. Eng. 245 (2024) 122858.
[14] W. Zeng, W. Sun, L. Guo, et al., Optical investigation on effects of diesel injection strategy on ammonia/diesel dual fuel combustion characteristics and flame development, Fuel 363 (2024) 131027.
[15] J. Liu, X. Wang, W. Zhao, et al., Effects of ammonia energy fraction and diesel injection parameters on combustion stability and GHG emissions characteristics in a low-loaded ammonia/diesel dual-fuel engine, Fuel 360 (2024) 130544.
[16] J. Zhang, Z. Zhao, A.M. Elbanna, et al., On ammonia/diesel dual-fuel combustion in optical engine, Fuel 367 (2024) 131452.
[17] X. Liu, Q. Wang, W. Zhong, et al., Optical diagnostics in impact of ammonia energy ratio and diesel split ratio on combustion process and flame propagation in an Ammonia-Diesel Dual-fuel engine, Fuel 364 (2024) 131074.
[18] A. Yousefi, H. Guo, S. Dev, et al., A study on split diesel injection on thermal efficiency and emissions of an ammonia/diesel dual-fuel engine, Fuel 316 (2022) 123412.
[19] S. Mi, H. Wu, X. Pei, et al., Potential of ammonia energy fraction and diesel pilot-injection strategy on improving combustion and emission performance in an ammonia-diesel dual fuel engine, Fuel 343 (2023) 127889.
[20] G. Hashimoto, K. Hadi, Y. Xia, et al., Turbulent flame propagation limits of ammonia/methane/air premixed mixture in a constant volume vessel, Proc. Combust. Inst. 38 (4) (2021) 5171–5180.
[21] C. Lhuillier, P. Brequigny, F. Contino, et al., Experimental study on ammonia/hydrogen/air combustion in spark ignition engine conditions, Fuel 269 (2020) 117448.
[22] J. Otomo, M. Koshi, T. Mitsumori, et al., Chemical kinetic modeling of ammonia oxidation with improved reaction mechanism for ammonia/air and ammonia/hydrogen/air combustion, Int. J. Hydrogen Energy 43 (5) (2018) 3004–3014.
[23] C. Shi, R. Duan, T. Cheng, et al., Understanding the role of ammonia combined injection in improving combustion and emissions characteristics for heavy-duty CI engine, Energy 324 (2025) 135959.
[24] C. Shi, T. Cheng, R. Duan, et al., An insight into the effects of injection pressure and nozzle dimension on combustion characteristics and pollutant formation of ammonia/diesel dual-fuel engines, Energy 329 (2025) 136784.
[25] R. Duan, Y. Zhu, H. Wang, et al., Evaluating the combustion process of a dual-fuel direct-injection engine considering ammonia injectors spatial modification, Appl. Therm. Eng. 283 (2026) 128971.
[26] H. Xu, J. Wang, C. Zhang, et al., Numerical study on laminar burning velocity of ammonia flame with methanol addition, Int. J. Hydrogen Energy 47 (65) (2022) 28152–28164.
[27] Y. Li, H. Li, H. Guo, et al., A numerical investigation on methane combustion and emissions from a natural gas-diesel dual fuel engine using CFD model, Appl. Energy 205 (2017) 153–162.
[28] K.J. Richards, P.K. Senecal, E.D. Pomraning, CONVERGE Manual (Version 2.3), Convergent Science Inc., Madison, WI, 2016.
[29] L. Xu, Y. Chang, M. Treacy, et al., A skeletal chemical kinetic mechanism for ammonia/n-heptane combustion, Fuel 331 (2023) 125830.
[30] H. Liu, J. Li, J. Wang, et al., Effects of injection strategies on low-speed marine engines using the dual fuel of high-pressure direct-injection natural gas and diesel, Energy Sci. Eng. 7 (5) (2019) 1994–2010.
[31] Z. Han, R.D. Reitz, Turbulence Modeling of Internal Combustion Engines using RNG κ-ε Models, Combust. Sci. Technol. 106 (4–6) (1995) 267–295.
[32] R.D. Reitz, J.C. Beale, Modeling Spray Atomization with the Kelvin-Helmholtz/Rayleigh-Taylor Hybrid Model, Atomization Sprays 9 (6) (1999) 623–650.
[33] O.O. Taskiran, M. Ergeneman, Trajectory based droplet collision model for spray modeling, Fuel 115 (2014) 896–900.
[34] P.J. O'Rourke, A.A. Amsden, A Spray/Wall Interaction Submodel for the KIVA-3 Wall Film Model, SAE Technical Paper, 2000, 2000-01-0271.
[35] W. Pan, C. Yao, G. Han, et al., The impact of intake air temperature on performance and exhaust emissions of a diesel methanol dual fuel engine, Fuel 162 (2015) 101–110.
[36] M. Treacy, L. Xu, H. Fatehi, et al., Performance of a methanol-fueled direct-injection compression-ignition heavy-duty engine under low-temperature combustion conditions, Energies 17 (17) (2024) 4307.